Applied Catalysis B: Environmental 146 (2014) 151–161

Contents lists available at ScienceDirect

Applied Catalysis B: Environmental

journal homepage: www.elsevier.com/locate/apcatb

Synergy effect in photodegradation of contaminants from water using ordered mesoporous carbon-based titania catalyst

Wei Wei, Chao Yu, Qingfei Zhao, Xufang Qian, Guisheng Li*, Ying Wan*

Key Laboratory of Resource Chemistry of Ministry of Education, Shanghai Key Laboratory of Rare Earth Functional Materials, and Department of Chemistry, Shanghai Normal University, Shanghai 200234, PR China

ARTICLE INFO

Article history:
Received 11 October 2012
Received in revised form 11 March 2013
Accepted 25 April 2013
Available online 3 May 2013

Keywords:
Adsorption–photocatalysis
Synergy
Carbon
Titania
Mesoporous

ABSTRACT

A synergy effect by carbon and anatase in the mesoporous C–TiO_2 nanocomposites is reported here on the degradation of dye in contaminated water. The as-formed mesoporous C–TiO_2 composites have ordered 2D hexagonal mesostructure, high surface area (384 m^2/g), uniform and large mesopores (4.5 nm), large pore volume (0.31 cm^3/g), titania nanoparticles confined inside carbon frameworks, tunable TiO_2 contents (40–87 wt%), and dopant of element carbon into anatase lattice. The large mesopore space of carbon offers high capacity for the adsorption of dyes from water. Well-dispersed and carbon-doped anatase TiO_2 nanoparticles are active for photocatalysis especially in visible light region. Once the dyes are involved inside mesopores by adsorption, they are easily accessible to anatase particles through the common interface between the two, and immediately fully oxidized. The immobilization of anatase particles in the carbon framework greatly improves the stability during its usage. The mesoporous C–TiO_2 nanocomposite catalysts can be reused more than 20 times without obvious loss both in anatase content and processing ability of contaminated water.

1. Introduction

The use of nanosized powders of TiO_2 in order to obtain a large surface-area-to-volume ratio, and therefore copious provision of active sites is well established practice, for example, the most frequently used commercial powders of P25 [1]. However, problems with the use of powders are also well recognized, specifically; (1) the loss of catalysts in the solution; (2) aggregation of particles in suspension, especially at high loadings; (3) difficulty in application to continuous flow systems [1,2]. Various supports have been adopted to fix nanosized TiO_2, including activated carbon [3–5], SiO_2 [6], ZrO_2 [7], zeolites, glass beads, stainless steels [8–10]. In particular, activated carbon (AC) has been extensively investigated as a support for heterogeneous catalyst.

Activated carbon with a porous amorphous structure can provide a high-surface area structure over which TiO_2 nanoparticles may be distributed and immobilized (typically 900–1200 m^2/g). Distribution techniques include mechanical mixing, aqueous suspensions [11], sol–gel [12], hydrothermal techniques [13,14], chemical vapor deposition [5,15,16], etc. The resulting AC–TiO_2 mixtures/composites are widely reported to yield improvements in photocatalytic activity over TiO_2 alone, attributed to the porosity of the support providing high adsorption capacity and ready passage of reacting species to the TiO_2 particles [15,17–19]. Secondly, the carbon support can improve the thermal stability of the composite, and therefore, resist the phase transformation from anatase to rutile or aggregation of anatase nanoparticles [20,21]. Thirdly, it has also been reported that the synergistic effect between the support and TiO_2 nanoparticles may also enhance the photocatalytic performance [17–19,22–25]. The synergistic effect is suggested to be possible because of weak interactions between the TiO_2 and AC support; detected by a slight change in pH_{PZC} in the composite. The synergistically improved photocatalytic activity may be explained by the adsorption of reactants on AC followed by mass transfer to the photoactive TiO_2 through the common interface between the two [17,18,23,25]. Because the adsorption rate is apparently slower by several order than recombination of photogenerated electron–hole pairs [26,27], the large surface area of activated carbon which can facilitate the adsorption of organic substances is responsible for the enhanced photocatalytic activity. As a consequence, these enhancements are obviously related to the porosities. Lastly but not least, the AC support itself is capable of a significant level of self-photocatalytic activity, actually out-performing the AC–TiO_2 composite under UV light irradiation [28]. The lower photocatalytic activity in the AC–TiO_2 is due to the drop in porosity of the composite, and blockage of the photoactive centers in the AC support after immobilization of TiO_2.

Activated carbons usually possess the porosity spanning the macro- (>50 nm), meso- (2–50 nm) and micro- (<2 nm) pore ranges [28]. The smaller pores are rarely infiltrated when dispersing TiO_2

* Corresponding authors. Tel.: +86 21 6432 2516; fax: +86 21 6432 2511.
E-mail address: ywan@shnu.edu.cn (Y. Wan).

0926-3373/$ – see front matter © 2013 Elsevier B.V. All rights reserved.
http://dx.doi.org/10.1016/j.apcatb.2013.04.048

nanoparticles, with the TiO_2 remaining on the outer macropores [28]. On one hand, porosity cannot be fully occupied to disperse nanoparticles, especially for microporous activated carbon. On the other hand, the random dispersion and size distribution of nanoparticles potentially leaves much of the nanoscale effect related to TiO_2 under exploited. Furthermore, the need for band-gap tuning of the TiO_2 which is fundamental issue in improving photocatalytic activity by carbon doping [29], remains un-tackled by use of activated carbon as a support that does not chemically interact with the TiO_2.

Ordered mesoporous carbons, which possess tunable and large pore sizes, high surface areas, periodically arranged monodispersed mesopore space, and alternative pore shapes, therefore provide a good opportunity to support the TiO_2 nanoparticles [30–32]. Recently, several groups including ours separately reported the formation of TiO_2–C nanocomposites. This kind of catalysts show ordered mesostructure, large pore sizes, high surface areas and large pore volumes. Anatase nanoparticles are well dispersed and immobilized inside the ordered mesoporous carbon frameworks without blockage of mesopores. However, the catalytic activity is lower by 1–2 order of magnitude in reaction rate than commercial P25 in dye degradation in solution under UV light [33]. The prominent "negative" effect by carbon support attracts our interest. Very recently, we found that a TiO_2–C composite with an anatase content of 60 wt% can behave an enhanced photocatalytic performance in degrading dye solution [32]. But the effect of titania content is not discussed.

In this manuscript, we present an adsorption–photocatalysis cycle to separate the adsorption and photocatalysis over mesoporous C–TiO_2 nanocomposites with TiO_2 contents ranging from 40 wt% to 87 wt%, and therefore highlight the role of carbon mesostructure and TiO_2 individually, and their synergy effect. The first role of carbon is dispersion and immobilization of anatase nanoparticles inside mesoporous framework, even with a high TiO_2 content of 87 wt%. High adsorption abilities are observed for all mesoporous C–TiO_2 nanocomposites, which are much related to the high BET surface area of carbonaceous materials. In the subsequent irradiation, a high efficiency in eliminating adsorbed dyes inside mesopores is obtained, due to the fact that the easy mass transfer of the dye to the photoactive TiO_2 through the common interface between the two. The separation of the adsorption and photocatalysis processes greatly improves the reaction rate. More importantly, the carbon element can be doped with anatase, playing a band-gap tuning role. The proposed route produced an excellent photocatalytic performance for degrading phenol under visible light irradiation, much higher than that of commercial P25.

2. Experimental

2.1. Synthesis of mesoporous C–TiO_2 nanocomposites (MCTs)

MCTs were synthesized by using $TiCl_4$ and/or $Ti(OC_4H_9)_4$ as titanium sources, water- and ethanol-soluble phenolic resin as the carbon source, and triblock poly (ethylene oxide)-b-poly (propylene oxide)-b-poly (ethylene oxide) copolymer F127 ($EO_{106}PO_{70}EO_{106}$, Mw = 12,600), or P123 ($EO_{20}PO_{70}EO_{20}$, Mw = 5800) as the structure-direct agent via the evaporation induced self-assembly (EISA) strategy [33,34]. The phenolic resin precursor was synthesized by a base-catalyzed polymerization of phenol and formaldehyde, as reported by the literatures [35]. Before use, $MgSO_4$ was used to remove the residual water in phenolic resin.

MCT-87: 1.4 g (7.4 mmol) of $TiCl_4$, 4.2 g (12.6 mmol) of $Ti(OC_4H_9)_4$, 0.68 g of resol solution which contains 0.24 g of phenol, 0.44 g of formaldehyde, and 1.4 g of ethanol were added into a clear solution with 2.0 g of P123 and 30 g of ethanol in sequence with stirring. An orange red solution was obtained. After 10 min, the mixture was poured into Petri dishes. Then, the dishes were placed in a hood to evaporate ethanol at ambient temperature in air and in an oven to thermopolymerize at 100 °C. Both the treatments took about 24 h. The as-made orange samples were collected and heated at 350 °C for 10 h to remove the triblock copolymer template. Further crystallization for titania was adopted at 550 °C for 30 min in nitrogen atmosphere. The heating rate was 1 °C/min below 350 °C and 5 °C/min above 350 °C. The sample was named as MCT-87 (the number denotes the wt% of titania).

MCT-60, and 40: solution A contains 1.5 g of F127, 1.0 g of deionized water and 8.0 g of ethanol which were stirred at 40 °C for 2 h. Stöber solution B contains 1.92 g (10.1 mmol) of $TiCl_4$, 0.5 g of deionized water and 7.5 g of ethanol which were stirred at 0 °C for 30 min. Solution A and B were mixed together, and the color turned into orange rapidly. After 30 min, the solution was mixed with 5.0 g of phenolic resol. The mixture was then poured into Petri dishes. The subsequent treatments were exactly the same as those for MCT-87. The calcined product was denoted as MCT-60. Tuning the $TiCl_4$ mass to 0.83 g (4.4 mmol), and F127 mass to 1.13 g, the final material was denoted as MCT-40.

To remove the free carbon component, the MCT-n sample was treated in a muffle oven at 350 °C for 9 h in air. The resultant white solid TiO_2-n was collected.

For comparison, pristine mesoporous carbon (MC) [36] and mesoporous titania (MT) [37] were also synthesized according to literatures (the detailed preparation procedures were described in Supporting Information, SI).

2.2. Characterization

The small-angle X-ray diffraction (XRD) measurements were taken on a Rigaku D/max B diffractometor using Cu Kα radiation (40 kV, 20 mA). The d-spacing values were calculated by the formula of $d = 0.15408/2\sin\theta$, and the unit cell parameters were calculated from the formula of $a_0 = 2d_{100}/\sqrt{3}$. N_2 adsorption–desorption isotherms were measured at 77 K with a Quantachrome NOVA 4000e analyzer. The Brunauer–Emmett–Teller (BET) method was utilized to calculate the specific surface areas (S_{BET}). By using the Barrett–Joyner–Halenda (BJH) model, the pore volumes and pore size distributions were derived from the adsorption branches of isotherms. The micropore volumes (V_m) were calculated from the V–t plot method. The t values were calculated as a function of the relative pressure using the de Boer equation, t (nm) = [0.1399/(log(p_0/p) + 0.0340)]$^{1/2}$. V_m was obtained using the equation of V_m (cm^3/g) = 0.001547I, where I represents the Y intercept in the V–t plot. Transmission electron microscopy (TEM) experiments were conduced on a JEOL 2011 microscope operated at 200 kV. The samples for TEM measurements were suspended in ethanol and supported onto a holey carbon film on a Cu grid. Energy dispersive X-ray spectroscopy (EDX) was performed on a Philips EDAX instrument. Thermal gravity analysis (TG) curves were monitored on a Mettler Toledo 851e apparatus. The C, H and O contents were measured on a Vario EL III elemental analyze (Germany). X-ray photoelectron spectroscopy (XPS) measurements were performed on a Perkin–Elmer PHI 5000CESCA system with a base pressure of 10^{-9} Torr. The energy positions of the peaks were calibrated by fixing the position of the C1s peak at 284.6 eV. The diffuse reflectance spectra of the samples over a range of 200–800 nm were recorded by a Varian Cary 300 Scan UV-vis system equipped with a Labsphere diffuse reflectance accessory.

2.3. Catalytic tests

The photocatalytic activity of the mesoporous carbon–titania composites (MCT-n) was characterized by measuring the titania

assisted photodegradation of the methylthionine chloride, and fuchsin basic.

For the dye degradation in solution, 0.05 g of composite catalyst was suspended in 50 mL of aqueous solution containing methylthionine chloride (c_0 = 50 mg/L). The suspensions were placed in dark before illumination to allow sufficient adsorption of methylthionine chloride. The reactor was irradiated by 300 W xenon lamp (AULTT CEL-HXF300) located directly above the vessel at a distance of 10 cm from the surface of the liquid or solid (in the case of adsorption–photocatalysis cycle). The UV–vis radiation ranges from 350 nm to 680 nm. The average incident photon flux at the interface (solution or solid catalyst) was measured to be 910 mW/cm^2. The visible irradiation was undertaken by a 420 nm cutoff filter. The average incident photon flux at the interface was measured to be 670 mW/cm^2. In some specific tests, the stirred suspensions were immediately illuminated without pre-adsorption. The change of the methylthionine chloride concentration with irradiation time was monitored by measuring the UV–vis absorption of the suspensions centrifuged at 4000 rpm to remove titania-containing mesoporous particles at different interval periods. The UV–vis absorption was measured on a UV-7502PC spectrometer, and the absorbance at the absorption maximum (664 nm) was used for the determination of the concentration of methylthionine chloride. Catalytic results are shown in terms of absolute conversion of dye. For kinetics study, 0.01 g of catalyst was used. Initial reaction rate was calculated on the basis of mmol reacted dye per mol TiO_2 and per min with a dye conversion less than 15%.

For the adsorption–photocatalysis cycles, 0.10 g of MCT-*n* was suspended in 100 mL of aqueous solution containing 0.4 g/L of methylthionine chloride or fuchsin basic. Then the mixture was continuously shaken in a shaking bath with a speed of 120 rpm at 25 °C until the equilibrium was reached (typically 24 h). After adsorption, an aliquot was centrifuged at 4000 rpm for 5 min and the dye concentration in the cleat supernatant was determined spectrophotometrically by measuring the absorbance of the solution with a UV–vis spectroscopy. The separated catalyst, loaded with dyes, was dried at 40 °C overnight under vacuum. The photocatalytic degradation of dye was initiated by irradiating the dye-loaded catalyst mixture with a commercial 300 W xenon lamp. The light source was located 10 cm from the solid surface. After 2 h, the lamp was turned off. This was one adsorption–photocatalysis run. The composite catalyst was then re-subjected to an aqueous solution containing dye (0.4 g/L) to complete the second run. The re-adsorption amount was counted as degradation concentration (c). Regeneration efficiency was calculated by $(c_m/c_{m-1}) \times 100\%$ wherein m was the times for adsorption–photocatalysis run. Preliminary tests demonstrated a good linear relationship between the light absorbance and the photocatalytic ability. Only less than 2% dye can be re-adsorbed in the composite catalyst if the first degradation step is in the absence of the light irradiation and, thus, could be neglected in comparison with the degradation via photocatalysis. Over 20 runs were carried out. All operations were exactly the same.

3. Results

Fig. 1A shows the TG curves of the MCT hybrids, which suggests that carbonaceous materials were burnt off around 300–500 °C, leaving 40–87 wt% inorganic solids. Accordingly, the titania content in the MCT composites was increased from 40 wt% to 87 wt% with the increase of total titanium content in the synthesis batch. It should be noted that the estimation is rough, neglecting the weight loss caused by the cross-linkage of inorganic species during the temperature range. Exothermic peaks can be observed together with the dominant weight loss. The area for the peak is in the order of MCT-40 > MCT-60 > MCT-87, further demonstrating the increase in the carbonaceous substances content of this order.

TEM images for mesoporous carbon–titania composites (Fig. 2) show typical images for an ordered mesostructure in large domains. HRTEM images reveal that the framework is composed of a large amount of nanoparticles and amorphous substance. The nanoparticles with sizes of about 5–8 nm are well arranged inside the pore walls and conglutinated by amorphous substance. The composite with a high TiO_2 content shows a large nanoparticle size. Notably, pore blockage is probably not serious, leaving large enough space for adsorption inside the straight channels. Similar results have also been reported in mesoporous solids based titania, in which nanocrystals are randomly "glued" together by amorphous substances such as carbon, P_2O_5, silica, etc. [27,33,38–40]. In large areas, the *d*-spacing of these nanocrystals is 0.35 nm, related to the (1 0 1) plane of anatase. The (0 0 4) plane of anatase with a *d*-spacing value of 0.24 nm can also be observed which are rarely reported in other anatase nanoparticles.

The small angle-XRD patterns for as-made mesoporous C–TiO_2 composites display (1 0 0) and (1 1 0) peaks (SI Fig. S1), displaying the ordered 2D hexagonal mesostructure. Upon calcination, the ordered mesostructure can be well retained, as evidenced by the well-resolved diffraction peak (Fig. 3A), confirming the TEM results. The cell parameters are calculated to be 10.9 nm, slightly smaller than those for the as-made composites, suggesting the

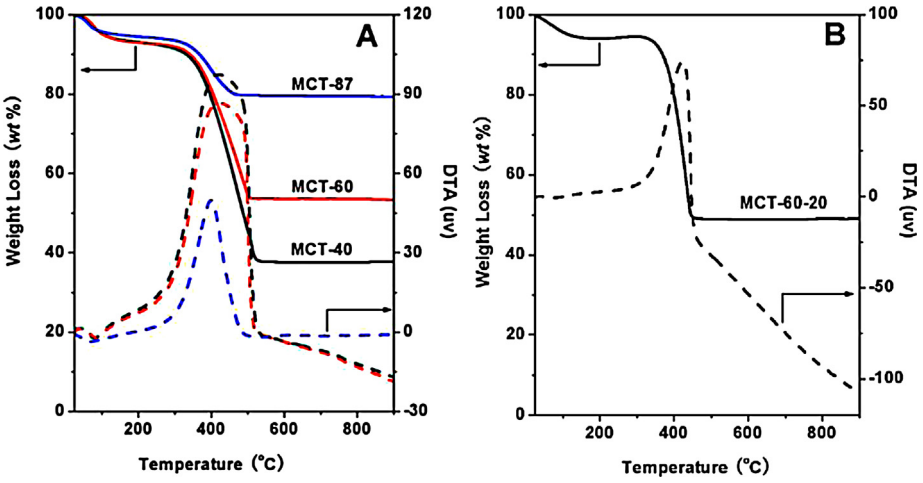

Fig. 1. TG/DTA curves carried out in air for (A) fresh mesoporous C–TiO_2 composites with TiO_2 contents of 40, 60 and 87 and (B) MCT-60 after 20 adsorption–photocatalysis cycles.

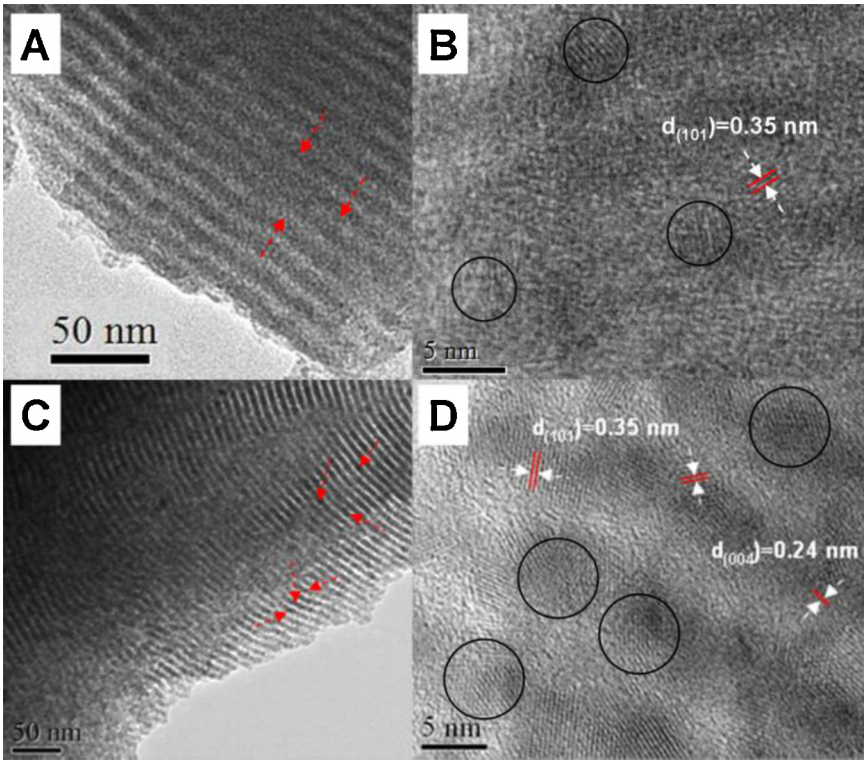

Fig. 2. (A) and (C) TEM and (B) and (D) HRTEM images for (A) and (B) MCT-60 and (C) and (D) MCT-87 viewed perpendicular to pore channels.

framework shrinkage. The diffused peaks at 2θ of 25, 38, 48 and 54° in the wide-angle XRD pattern for MCT-60 and MCT-87 can be ascribed to the (1 0 1), (0 0 4), (2 0 0) and (2 1 1) facets of anatase, implying the highly dispersion of crystalline nanoparticles and tiny size (Fig. 3B). According to the line width analysis of the (1 0 1) reflection based on the Scherrer formula, average crystallite sizes for the MCT-60 and MCT-87 composites are estimated to be about 4.2 and 5.4 nm, respectively. The unresolved peaks at 2θ of about 23 and 43° which are overlapped with the diffractions belonging to anatase can be assigned to amorphous carbon. Only the peaks of amorphous carbon can be detected for the catalysts MCT-40. These observations demonstrate that the catalyst contains tiny anatase nanoparticles and amorphous carbon, and the particle size increases with the increase in the TiO_2 content.

XPS spectra (Fig. 4) for the MCT composites show the spectral Ti $2p_{3/2}$ and Ti $2p_{1/2}$ values comparable to bulk; but the spin-orbital splitting is 5.6 eV, regardless of TiO_2 contents, slightly lower than both bulk anatase and neat mesoporous titania (5.8 eV) (SI Fig. S2) [41]. This observation has also been reported for non-metal doped anatase, and been attributed to the hybrid atom introduction in

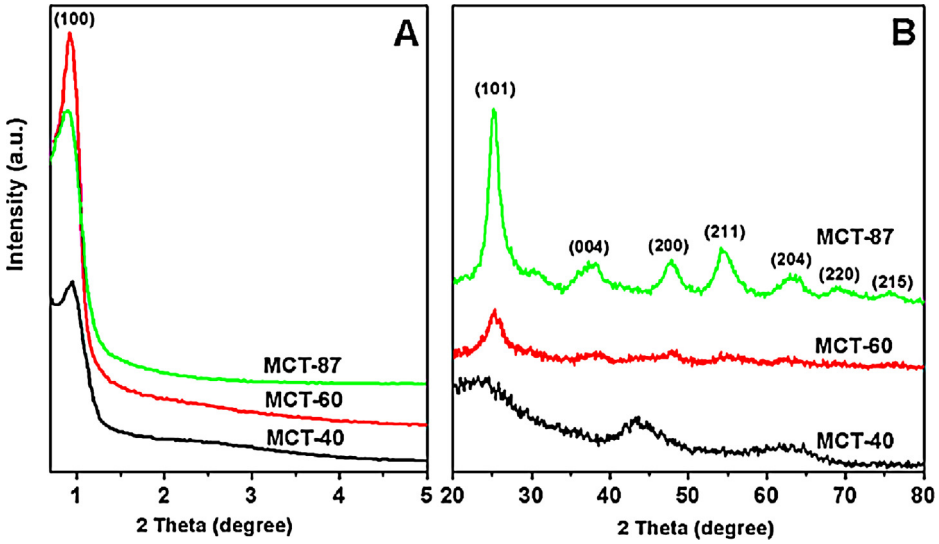

Fig. 3. Small-angle (A) and wide-angle (B) XRD patterns for mesoporous C–TiO_2 nanocomposites with different TiO_2 contents synthesized via the evaporation induced self-assembly approach.

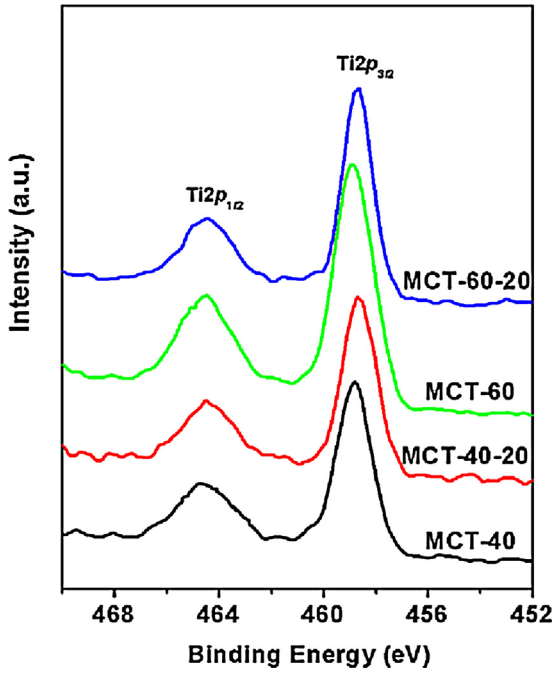

Fig. 4. XPS spectra for (A) MCT-40 and (B) MCT-60 before and after 20 adsorption–photodegradation cycles.

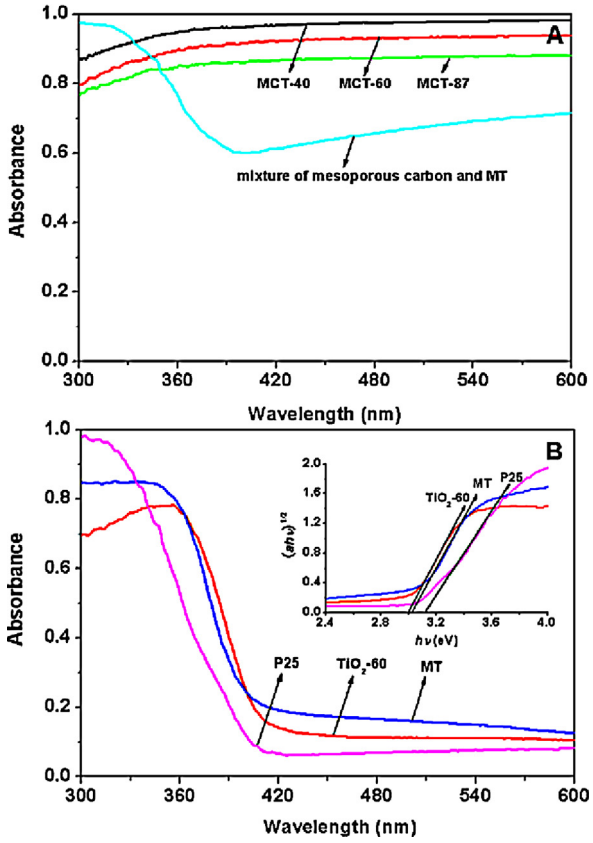

Fig. 5. Diffuse reflectance UV–vis spectra for (A) black powders mesoporous carbon–titania composites with different TiO_2 contents, and physical mixture of mesoporous carbon and mesoporous titania; and (B) white powders of TiO_2-60 which is a descendant of MCT-60 by combustion of free carbon, neat mesoporous TiO_2, and commercial P25. Inset (B) is modified Kubelka–Munk function.

the anatase crystal lattice [42]. No signals belonging to the TiC material at 454.9 and 460.7 eV can be detected, in good agreement with the XRD patterns. The carbon element doping in TiO_2 lattice thus is responsible for the change in spin-orbital splitting. The change of surface electric charge of the oxides in the carbon–titania composite catalysts may lead to modifications of the fundamental process of electron/hole pair formation while applying visible irradiation, which has been proved to enhance the photocatalytic performance under visible light [41,43–45]. The spin-orbital splitting for Ti $2p_{3/2}$ and Ti $2p_{1/2}$ XPS spectral values of both MCT-40 and MCT-60 are not changed after reaction cycles, suggesting the stability in hybrid atom introduction, and thus changes in surface electric charge.

The UV–vis spectra were further used to evaluate the carbon modification of TiO_2 (Fig. 5). Neat mesoporous TiO_2 has no absorption above its fundamental absorption sharp edge rising at 400 nm. By comparison, the titania particles TiO_2-60 which is derived from the MCT-60 nanocomposite catalyst can absorb light at higher wavelengths than that of neat TiO_2. The enhanced absorption observed in the visible region can be attributed to the introduction of carbon element in the anatase lattice [46,47]. A plot of the modified Kubelka–Munk function versus the energy of exciting light [48,49] affords bandgap energies of 2.99, 3.15, and 3.05 eV for TiO_2-60, P25, and neat mesoporous titania, respectively (this corresponds to absorption onsets of 415, 394, and 404 nm). The maximum band-gap narrowing of TiO_2-60 is comparable with the value of 0.14 and 0.05 eV observed for carbon-doped and nitrogen-doped TiO_2 [47,50,51], further confirming the element carbon introduction into the TiO_2 lattice in the carbon-anatase composite.

It should also be mentioned that mesoporous carbon–titania composites enhance the absorption over the whole UV to visible region, even with a high titania content of 87 wt%. This phenomenon is different with the carbon-based anatase catalysts such as amorphous carbon, carbon nanotube, and carbon nanofiber, on which the strong absorption is relevant with the titania content [27,52–54].

When the content of carbon substances in the composite is below 40%, both the absorption of anatase and carbon are predominant [27,52]. In the supported catalysts, titania large particles may exist on the outer macropores or surface of carbon materials, with the small pores rare infiltration [28]. Accordingly, the absorption by TiO_2 can be prominent with a high content in the catalysts. In addition, the mixture of black mesoporous carbon and neat mesoporous TiO_2 with the mass ratio of 20:80 show two apparent absorption, belonging to anatase and carbon, respectively. These observations demonstrate that the mesoporous carbon–titania nanocomposites are structurally different either with the physical mixture of mesoporous carbon and titania, or activated carbon and multiwall carbon nanotubes supported TiO_2 particles. The light absorption of anatase is shielded by carbon in the mesoporous composites, even with an extremely low-content carbon support, due to the high dispersion and immobilization of anatase TiO_2 nanoparticles by carbon pore walls.

The calcined MCT materials yield a type IV isotherms with a sharp capillary condensation step at middle relative pressures (p/p_0 = 0.4–0.6), and an H2-type hysteresis loop is observed, suggesting the roughly cylindrical pores, possibly resulted from the different shrinkage between inorganic material and phenolic resins and the evaporation method (Fig. 6) [55–57]. Desorption branches are delayed to relative pressures close to the fluid cavitation pressure. A narrow pore size distribution with a mean value of about 4.0 nm is calculated from the adsorption branch by the BJH method. Although the BJH model has recently been found somewhat problem to calculate the pore size, it has been widely adopted in the

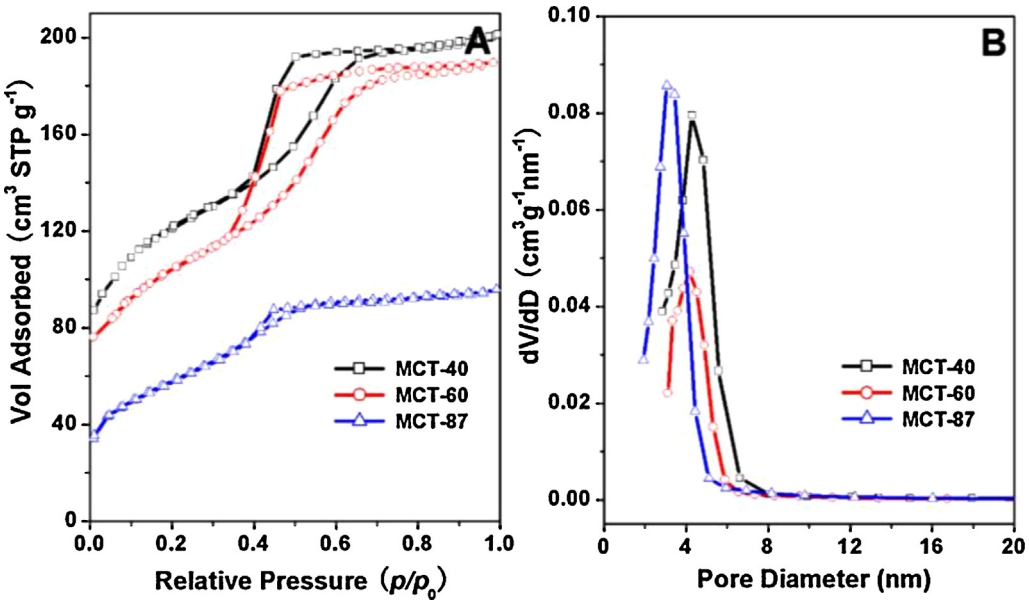

Fig. 6. (A) Nitrogen sorption isotherms and (B) pore-size distribution curves for mesoporous C–TiO_2 composites with different TiO_2 contents after crystallization at 550 °C in N_2 flow.

mesostructured materials community for comparison. The calcined mesoporous materials have BET surface areas ranging from 207 m^2/g to 384 m^2/g and pore volumes ranging from 0.15 cm^3/g to 0.31 cm^3/g (Table 1).

The photocatalytic activity of the mesoporous C–TiO_2 composites with different TiO_2 contents was examined by measuring the photodegradation of methylthionine chloride (c_0 of 50 mg/L) in an aqueous suspension. The mesoporous composites show high adsorption ability for methylthionine chloride. The residue dye (c/c_0) is as low as 8–15% after 24 h adsorption depending on the catalyst used (SI Fig. S3 and Fig. 7A). In the literatures [23], the apparent kinetic constant was selected to compare the catalytic behavior of the different catalysts and substances. The initial concentrations were considered those measured when the lamp was turned on, after stirring of the suspension in the dark. In the present case, the distinct reduce in dye concentration is observed by adsorption in mesoporous C–TiO_2. The disappearance of the dye in the solution occurs within 5 min after the light on, displaying the apparent kinetic constants much higher than P25 (0.1669 min^{-1}).

Samples were then initially mixed with methylthionine chloride (50 mg/L), and immediately illuminated by UV–vis light. Within 90 min, the dye in aqueous solution cannot be detected (Fig. 7B). Negligible TOC concentration in the decant water can be detected for mesoporous C–TiO_2 catalysts, implying the mineralization of dyes. Since the adsorption and photocatalysis simultaneously occurs over mesoporous C–TiO_2 composites, the catalysts after reaction are washed by 10 mL of ethanol under ultrasonic for 3 times which had been reported to be an efficient method to elute organic substances inside carbon mesopores [58]. Negligible dye was eluted, indicating that the dye both in the solution and inside pores had been degraded. Although the estimation is rough, neglecting the possible residue of dye inside pores even after elution and the oxidation of dye to large carbonaceous molecules, the result may reflect the relative reaction rate. The dye reduction constant for catalysts MCT-40 (0.0933 min^{-1}) and MCT-60 (0.0521 min^{-1}) are lower than that for commercial P25 (SI Fig. S4). When initial apparent disappearance rate of methylthionine chloride is considered, MCT-60 also shows a lower initial reaction rate on the basis of the per mol anatase (0.878 mmol reacted dye $mol^{-1}(TiO_2)\,min^{-1}$) than P25 (1.66 mmol reacted dye $mol^{-1}(TiO_2)\,min^{-1}$). Inhibition of the TiO_2 catalytic behavior especially in MCT-60 is similar to that reported by Liu et al. [33], but obviously opposite with the titania coated activated carbon catalysts [17–19,22–25]. This phenomenon implies that the present mesoporous carbon-anatase nanocomposites are structurally different with the reported activated carbon–TiO_2 mixtures by use of activated carbon as a support.

We further tested the photocatalytic performance under visible light for the TiO_2-containing composite catalysts (Fig. 7C). The adsorption possibility for samples MCT-40 and MCT-60 was also ruled out by ethanol elution after photocatalysis. Both MCT-60 and MCT-40 catalysts are much more active than P25, and show a nearly complete TOC degradation. The improvement of the dye reduction constants is estimated to be 10 times. Such phenomenon implies the "positive" role in carbonaceous mesostructure on the photocatalytic performance of TiO_2.

To prove the catalytic activity of anatase particles which are immobilized in the carbonaceous framework, the free carbon was burnt off to leave TiO_2 particles. Upon combustion of MCT-60 at

Table 1
Structural and textural properties for mesoporous C–TiO_2 composites with different TiO_2 contents synthesized via the EISA approach.

Catalyst	TiO_2 content[a] (wt%)	a_0(nm)	S_{BET}(m^2/g)	V_t(cm^3/g)	V_{micro}(cm^3/g)	D_p(nm)
MCT-40	40	10.7	384	0.31	0.090	4.5
MCT-60	60	10.9	348	0.30	0.041	4.3
MCT-87	87	11.2	207	0.15	0.015	3.2
MT	100	12.5	129	0.22	0.002	5.5
MC	0	9.7	757	0.55	0.210	4.5

[a] Estimated from the TG analysis.

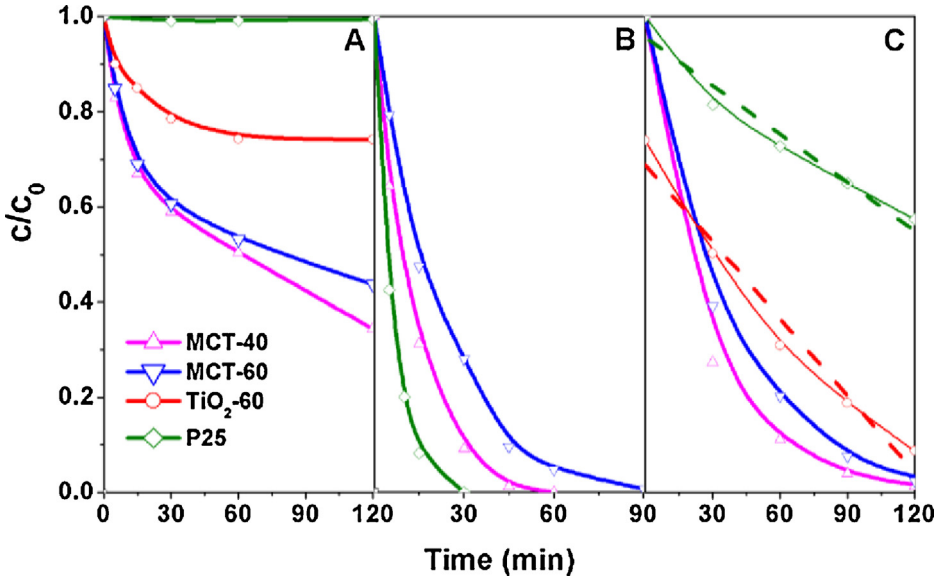

Fig. 7. Solution degradation of methylthionine chloride under (B) UV–vis light and (C) visible light over mesoporous C–TiO_2 nanocomposites with different TiO_2 contents, commercial P25, and a TiO_2 catalyst which is derived from MCT-60 by burning off the free carbon. The dash line in (C) is linear fit for c/c_0 versus time. For comparison, the adsorption in dark is also given in (A). For P25 and TiO_2-60 catalysts, a pre-adsorption for equilibrium adsorption are carried out before light on. For mesoporous C–TiO_2 nanocomposites, the light is turned on immediately after the solid catalyst was mixed with the solution.

350 °C in air, the resultant solid TiO_2-60 exhibits predominant diffractions of anatase, likely either because of the particle growth upon combustion or the elimination of shielding by amorphous carbon. It should be noted that the peaks are rather wide, reflecting the nanoparticles with sizes below 5.5 nm. TG analysis reveals the elimination of free carbon in TiO_2-60 (data not shown here). This catalyst shows a much higher reduction apparent rate than commercial P25 at degrading methylthionine chloride under visible light irradiation, indicating that the anatase nanoparticles are active (Fig. 7C).

An adsorption–photocatalysis cycle was carried out to separate the adsorption and degradation processes. The mesoporous composite was adopted as an adsorbent in polluted water with a relatively high dye concentration (c_0). Fig. 8A plots the adsorption capacities for methylthionine chloride over various C–TiO_2 materials as a function of the contacting time. A predominant increase in the initial period is found, indicating a fast adsorption. This phenomenon demonstrates the high affinity between the adsorbate and the adsorbent. But the adsorption equilibrium reaches with a long contacting time (24 h). High adsorption capacities are obtained for the mesoporous materials, indicating the avoidance of pore blockage by anatase nanoparticles and the accessible of pore space. The saturated adsorption amount is highly related to the BET surface area of the mesoporous composites. MCT-40 with a high BET surface area exhibits the large adsorption capacity.

After separation with water, the solid was directly irradiated under UV–vis light. Then, the used composite catalyst was subjected to the subsequent adsorption again. The re-adsorption amount was estimated as the degradation concentration (c).

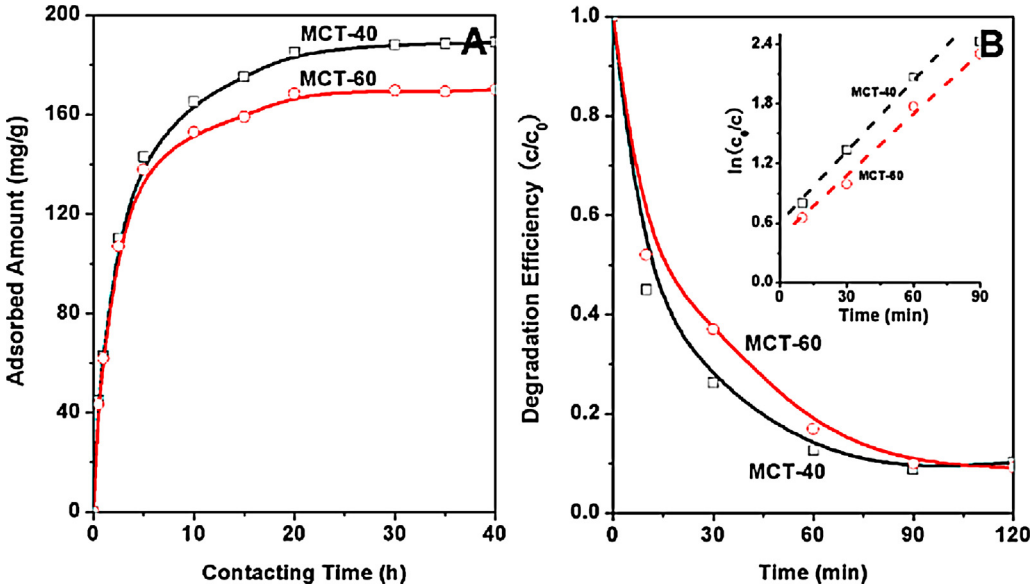

Fig. 8. Adsorption capacities (A) and degradation efficiency (B) for methylthionine chloride on the catalysts MCT-60 and MCT-40 as a function of the contacting time. Inset is kinetic curves with transformed linear graphs of $\ln(c_0/c)$ versus irradiation time.

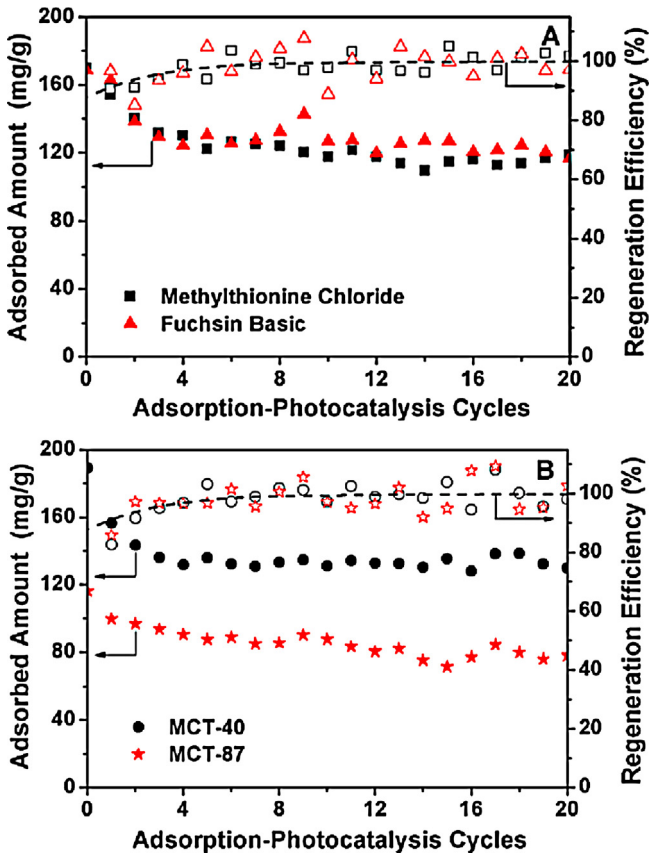

Fig. 9. Adsorption capacity for mesoporous C–TiO_2 catalysts with different TiO_2 contents in repeated adsorption–photocatalysis cycles which involves adsorption in polluted water containing methylthionine chloride and fuchsin basic with the initial concentration of 400 mg/L and photodegradation under UV–vis light: (A) MCT-60 for treating methylthionine chloride and fuchsin basic; (B) MCT-40 and MCT-87 for treating methylthionine chloride.

The dye involved in pores is degraded upon prolonging the illumination time, and reaches a constant after 2 h of reaction (Fig. 8B). The pseudo-first-order reaction is observed for both MCT-40 and MCT-60, with the dye reduction apparent constant of 0.0225 and 0.0214 min^{-1}, respectively. To confirm the photodegradation of dye by anatase nanoparticles in the composite catalysts, some parallel experiments were also carried out. The catalyst loaded with dyes which was placed for 8 h under dark is subjected to further adsorption of methylthionine chloride. The amount is about as low as 4 mg/g. A titania-free material, i.e. mesoporous carbon is also used as the catalyst. Mesoporous carbon exhibits a high adsorption capacity of 540 mg/g, but an extremely low second-step capacity of 14 mg/g after illumination under UV–vis light for 2 h. These observations illustrate that the dyes adsorbed in mesoporous carbon–titania composites can be degraded by anatase nanoparticles inside carbon pore walls under light. Once the dyes in pores are mineralized, the occupied pores are empty, thus, enough space can be provided again for re-adsorption.

The adsorption–catalysis cycles were then carried out for degrading methylthionine chloride and fuchsin basic over mesoporous composite catalysts with different TiO_2 contents, and repeated for 20 times (Fig. 9). Large adsorption amounts can be detected for each run. The difference in adsorption amount occurs in the first several cycles, and after 10 cycles, minor differences can be observed, regardless of the TiO_2 content and dyes. The regeneration efficiency is close to 100%, indicating the high stability of the composite catalyst.

The re-used solid catalyst MCT-60 after 20 cycles after the adsorption of dye in the 21th run was put into 50 mL of water for further degradation under UV–vis light. Negligible TOC concentration in the decant water can be detected after 4 h, implying the mineralization of dyes or the under detected-line concentration of organic intermediates. The solid was separated for further adsorption of dye. A similar re-adsorption capacity can be found with that in the 20th adsorption, indicating the almost complete TOC degradation by the composite catalyst. These results demonstrate that the loaded dyes inside mesopores can be fully oxidized to CO_2 due to the adsorption of intermediates if any and high catalytic performance by anatase nanoparticles.

The MCT-60 composite after 20 adsorption–photocatalysis cycles displays a weight loss of 44.3%, respectively, in the temperature ranging from 200 °C to 500 °C in the TG curve, higher than the fresh catalysts (Fig. 1B), implying the combustible substances residue inside mesopores of the composite after use. The residue organic compounds may include un-reacted dyes, large organic molecules or carbon deposition. Considering the difference of the adsorption ability between the first and 20th adsorption, the residue organic substances in the mesopores are about 50 mg/g for MCT-60. Accordingly, the carbon and titania contents in the MCT-60 composites after 20 runs are calculated to be about 39: 61, almost the same as the fresh catalysts. This illustrates the stable composites with negligible leaching of anatase nanoparticles in successive reaction cycles.

After 20 cycles of adsorption and photocatalysis, TEM images show that well dispersed nanoparticles with sizes about 4.2 nm are confined by pore walls of the ordered mesostructure, indicating the stable 2D hexagonal mesostructure and aggregation-free titania nanoparticles (Fig. 10). The used catalysts MCT-40 and MCT-60 after 20 cycles display similar diffraction peaks and unit cell parameter in both the small-angle and wide-angle XRD patterns with the fresh catalysts, indicating the stability of the mesostructure, and the reservation of anatase nanoparticles (Fig. 11).

4. Discussion

In the carbon–titania composites, the anatase nanoparticles are well arranged in the carbon mesopore walls, and accessible to the dyes adsorbed inside pores. The active center in MCT for photodegradation is anatase, and stable during reaction. Since anatase is UV sensitive semi-conductor (E_b = 3.2 eV, λ = 390 nm), the light sensitivity into the visible region the TiO_2-60 catalyst is probably attributed to the tuning of band-gap by element doping which has been confirmed by the XPS and UV–vis spectra analysis. The interstitial carbon atoms have been proven to improve the separation extent and restrain the recombination of the photo-induced electron and hole carriers in carbon-doped TiO_2, which is beneficial to improve the photocatalytic ability of catalysts [41]. The doping of element carbon into anatase lattice may be originated by the chelating between hydroxyl groups and titanium ions through strong intermolecular hydrogen-bonding interaction in the synthesis and the subsequent crystallization and carbonization accompanied with the formation of a large number of TiO_2 nanoparticles precipitates and the cleavage of Ti—O—C bonds [42,44].

The composite catalysts exhibit a similar or even slightly higher apparent dye degradation rate under UV than visible light, that is different with most research, in which anatase show much higher photocatalytic activity in UV light than in visible light. Compared with P25, the catalyst MCT-60 shows a “negative” role in performance under UV–vis irradiation and a “positive” role under visible light. These phenomena may be related to mass transfer, which

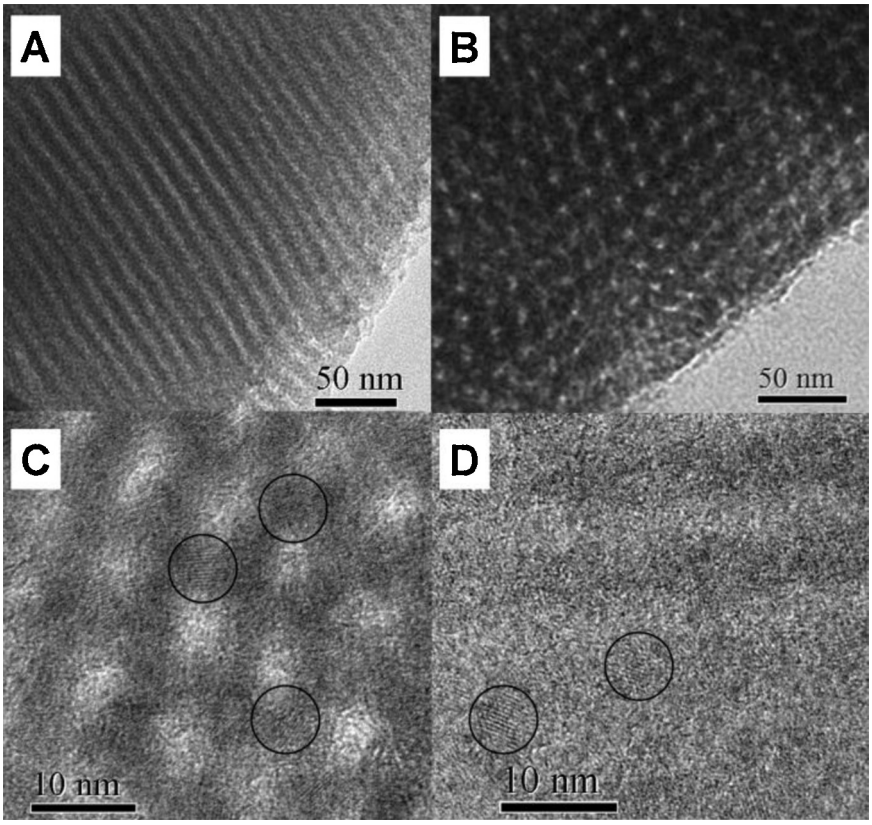

Fig. 10. TEM (A) and (B) and HRTEM (C) and (D) images of MCT-60 after 20 adsorption–photocatalysis cycles.

should be the rate determination step. The adsorption of dye inside mesopores is rather slow. Once the dyes are involved inside pores, anatase nanoparticles are effective to convert dye through the common interface between the two.

The determined mass transfer step can explain that MCT-40 with a low TiO_2 content but a high surface area exhibits a high dye degradation apparent rate than MCT-60 with a TiO_2 content of 60% and a relatively low BET surface area. Herein, we cannot exclude the orifice poisoning. The anatase nanoparticles at orifice are most active. Oxidative carbonaceous intermediates are firstly formed, and cannot transfer. The as-formed large molecules would cover the surface of TiO_2, the orifice reduction would also inhibit mass transportation, and therefore, lower the degradation rate constant. This phenomenon is prominent in the catalyst with a high TiO_2 content.

Lastly, the carbon–titania composite takes great advantages in stabilizing anatase nanoparticles compared to those activated carbon supported TiO_2 catalysts, in which metal leaching and particle

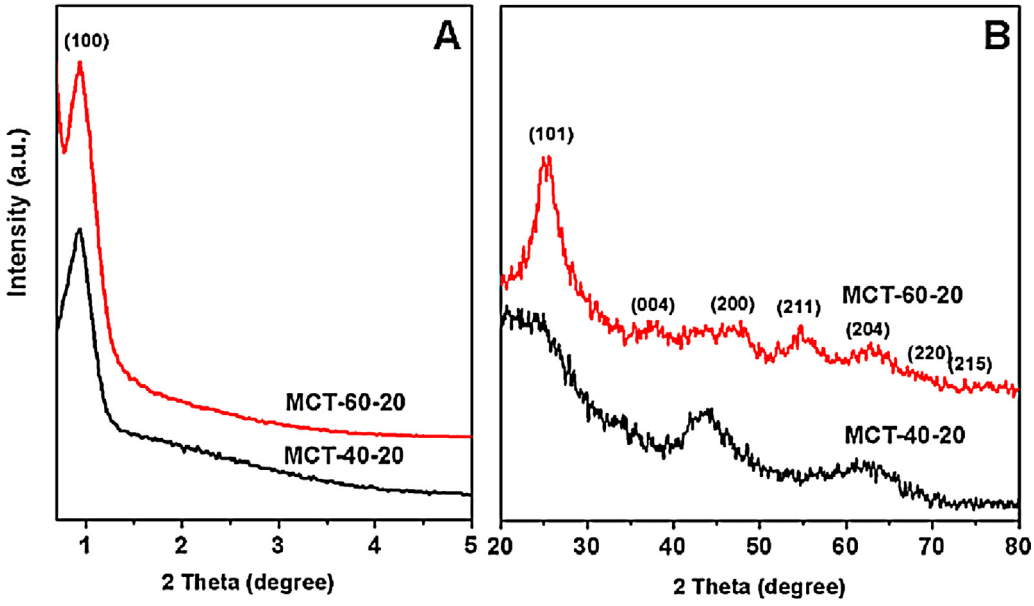

Fig. 11. Small-angle (A) and wide-angle (B) XRD patterns for MCT-40 and MCT-60 after 20 adsorption–photocatalysis cycles.

aggregation may become serious problems [38,59]. The high stability is probably due to the presence of the carbon framework which both shows stability in solution reaction and the "glue" role for anatase nanoparticles. The particles would be confined by the carbon pore wall, and therefore, inhibited by aggregation to large particles, provided that the carbon mesostructure is preserved.

The present adsorption–catalysis cycles separate the adsorption and photocatalysis processes. The avoidance of mass transfer inside mesopores in photodegradation and full accessibility of anatase nanoparticles facilitate the degradation of dye. In addition, the high adsorption ability of the mesostructure can adsorb the toxic intermediates, if formed. They are not released in the air atmosphere and/or in solution phase, and thereby preventing secondary pollution by the intermediates [60]. Therefore, such kind of cycles paves a good way for the treatment of organic contaminants with relatively high concentration.

5. Conclusions

To highlight the improved performance for anatase by carbon mesostructure, the mesoporous carbon–titania composite is applied as an adsorbent-catalyst to eliminate dye from water using both artificial UV and visible light. The adsorption and photocatalytic degradation processes are separated. The composite catalysts show a synergy effect by carbon and anatase on elimination of dye from water: the large mesopore size and space facilitate the adsorption of dyes with a high concentration, well dispersed anatase nanoparticles are active to convert dye through the common interface between the two, the carbon doping into the anatase lattice during the formation of the nanocomposite enhances the photocatalytic performance especially under visible light, and the carbon framework stabilizes the anatase nanoparticles with negligible leaching and aggregation during processes. The undetectable oxidative intermediates highlight the synergy effect. The heterogeneous supported catalysts are highly stable without obvious loss in TiO_2 weight and catalytic activity in the successive adsorption–photocatalysis cycles. About 100% adsorbed dyes including methylthionine chloride (about 120 mg/g), and fuchsin basic (about 125 mg/g) can be fully mineralized in 2 h under UV–vis light even after 20 cycles. The present adsorption–catalysis paves a good way for the treatment of organic contaminants with relatively high concentration.

Acknowledgements

This work was supported by State Key Basic Research Program of PRC (2013CB934102), Program for Changjiang Scholars and Innovative Research Team in University (IRT1269), MOE (20123127110004), NSFC (21073122, 21007040, and 21173149), Shanghai Sci. & Tech. and Edu. Committee (11JC1409200, 11SG42, S30406 and DZL123), and the Fok Ying Tung Education Fund (121013).

Appendix A. Supplementary data

Supplementary data associated with this article can be found, in the online version, at http://dx.doi.org/10.1016/j.apcatb.2013.04.048.

References

[1] R. Leary, A. Westwood, Carbon 49 (2011) 741–772.
[2] I. Sopyan, M. Watanabe, S. Murasawa, K. Hashimoto, A. Fujishima, Journal of Photochemistry and Photobiology A: Chemistry 98 (1996) 79–86.
[3] F. Rodríguez-reinoso, Carbon 36 (1998) 159–175.
[4] R. Ocampo-Pérez, M. Sánchez-Polo, J. Rivera-Utrilla, R. Leyva-Ramos, Applied Catalysis B: Environmental 104 (2011) 177–184.
[5] G. Li Puma, A. Bono, D. Krishnaiah, J.G. Collin, Journal of Hazardous Materials 157 (2008) 209–219.
[6] H. Miyata, Y. Fukushima, K. Okamoto, M. Takahashi, M. Watanabe, W. Kubo, A. Komoto, S. Kitamura, Y. Kanno, K. Kuroda, Journal of the American Chemical Society 133 (2011) 13539–13544.
[7] M. Chee Kimling, N. Scales, T.L. Hanley, R.A. Caruso, Environmental Science and Technology 46 (2012) 7913–7920.
[8] A. Fernández, G. Lassaletta, V.M. Jiménez, A. Justo, A.R. González-Elipe, J.M. Herrmann, H. Tahiri, Y. Ait-Ichou, Applied Catalysis B: Environmental 7 (1995) 49–63.
[9] E. Valova, J. Georgieva, S. Armyanov, S. Sotiropoulos, A. Hubin, K. Baert, M. Raes, Journal of the Electrochemical Society 157 (2010) D309–D315.
[10] M. Uzunova, M. Kostadinov, J. Georgieva, C. Dushkin, D. Todorovsky, N. Philippidis, I. Poulios, S. Sotiropoulos, Applied Catalysis B: Environmental 73 (2007) 23–33.
[11] J. Arana, R.J.M. Dona, O. Gonzalez Diaz, M.J.A. Herrera, J. Perez Pena, R.S. Malato, G.J. Blanco, Journal of Solar Energy Engineering 129 (2007) 80–86.
[12] M. Kubo, H. Fukuda, X.J. Chua, T. Yonemoto, Industrial and Engineering Chemistry Research 46 (2007) 699–704.
[13] S.X. Liu, X.Y. Chen, X. Chen, Journal of Hazardous Materials 143 (2007) 257–263.
[14] O.K. Mahadwad, P.A. Parikh, R.V. Jasra, C. Patil, Environmental Technology 33 (2011) 307–312.
[15] X. Zhang, M. Zhou, L. Lei, Carbon 44 (2006) 325–333.
[16] C.S. Kuo, Y.H. Tseng, C.H. Huang, Y.Y. Li, Journal of Molecular Catalysis A: Chemical 270 (2007) 93–100.
[17] B. Tryba, A.W. Morawski, M. Inagaki, Applied Catalysis B: Environmental 41 (2003) 427–433.
[18] Y. Ao, J. Xu, D. Fu, C. Yuan, Carbon 46 (2008) 596–603.
[19] J. Matos, J. Laine, J.M. Herrmann, Journal of Catalysis 200 (2001) 10–20.
[20] Z. Wang, N.S. Ergang, M.A. Al-Daous, A. Stein, Chemistry of Materials 17 (2005) 6805–6813.
[21] D. Zhang, D. Yang, H. Zhang, C. Lu, L. Qi, Chemistry of Materials 18 (2006) 3477–3485.
[22] J. Matos, J. Laine, J.-M. Herrmann, Applied Catalysis B: Environmental 18 (1998) 281–291.
[23] J. Araña, R. Doña, X. Amp, J.M. guez, E. Tello Rendón, C. Garriga i Cabo, D. González, O. Az, J.A. Herrera-Melián, J. Pérez-Peña, G. Colón, O.J.A. Navı, Applied Catalysis B: Environmental 44 (2003) 161–172.
[24] T. Cordero, J.-M. Chovelon, C. Duchamp, C. Ferronato, J. Matos, Applied Catalysis B: Environmental 73 (2007) 227–235.
[25] B. Tryba, International Journal of Photoenergy (2008), http://dx.doi.org/10.1155/2008/721824.
[26] M.R. Hoffmann, S.T. Martin, W. Choi, D.W. Bahnemann, Chemical Reviews 95 (1995) 69–96.
[27] K. Woan, G. Pyrgiotakis, W. Sigmund, Advanced Materials 21 (2009) 2233–2239.
[28] L.F. Velasco, J.B. Parra, C.O. Ania, Applied Surface Science 256 (2010) 5254–5258.
[29] D. Dolat, N. Quici, E. Kusiak-Nejman, A.W. Morawski, G. Li Puma, Applied Catalysis B: Environmental 115–116 (2012) 81–89.
[30] R. Ryoo, S.H. Joo, M. Kruk, M. Jaroniec, Advanced Materials 13 (2001) 677–681.
[31] Z. Wu, P.A. Webley, D. Zhao, Langmuir 26 (2010) 10277–10286.
[32] W. Wei, C. Yu, Q.F. Zhao, G.S. Li, Y. Wan, Chemistry: A European Journal (2012), http://dx.doi.org/10.1002/chem.201202691.
[33] R. Liu, Y. Ren, Y. Shi, F. Zhang, L. Zhang, B. Tu, D. Zhao, Chemistry of Materials 20 (2007) 1140–1146.
[34] X. Qian, Y. Wan, Y. Wen, N. Jia, H. Li, D. Zhao, Journal of Colloid and Interface Science 328 (2008) 367–373.
[35] Y. Wan, H. Wang, Q. Zhao, M. Klingstedt, O. Terasaki, D. Zhao, Journal of the American Chemical Society 131 (2009) 4541–4550.
[36] X. Zhuang, Y. Wan, C.M. Feng, Y. Shen, D.Y. Zhao, Chemistry of Materials 21 (2009) 706–716.
[37] B. Tian, X. Liu, B. Tu, C. Yu, J. Fan, L. Wang, S. Xie, G.D. Stucky, D. Zhao, Nature Materials 2 (2003) 159–163.
[38] P. Chang, C. Huang, R. Doong, Carbon 50 (2012) 4259–4268.
[39] W. Dong, Y. Sun, C.W. Lee, W. Hua, X. Lu, Y. Shi, S. Zhang, J. Chen, D. Zhao, Journal of the American Chemical Society 129 (2007) 13894–13904.
[40] D. Li, H. Zhou, I. Honma, Nature Materials 3 (2004) 65–72.
[41] Y. Cong, X. Li, Y. Qin, Z. Dong, G. Yuan, Z. Cui, X. Lai, Applied Catalysis B: Environmental 107 (2011) 128–134.
[42] W. Ren, Z. Ai, F. Jia, L. Zhang, X. Fan, Z. Zou, Applied Catalysis B: Environmental 69 (2007) 138–144.
[43] D. Chen, Z. Jiang, J. Geng, Q. Wang, D. Yang, Industrial and Engineering Chemistry Research 46 (2007) 2741–2746.
[44] X.Y. Zhang, H.P. Li, X.L. Cui, Y. Lin, Journal of Materials Chemistry 20 (2010) 2801–2806.
[45] Y.F. Li, D. Xu, J.I. Oh, W. Shen, X. Li, Y. Yu, ACS Catalysis 2 (2012) 391–398.
[46] T. Tachikawa, S. Tojo, K. Kawai, M. Endo, M. Fujitsuka, T. Ohno, K. Nishijima, Z. Miyamoto, T. Majima, Journal of Physical Chemistry B 108 (2004) 19299–19306.
[47] Y. Xu, Y. Zhuang, X. Fu, Journal of Physical Chemistry C 114 (2010) 2669–2676.
[48] Y. Tseng, C. Kuo, C. Huang, Y. Li, Zeitschrift fur Physikalische Chemie 224 (2010) 843–856.
[49] J. Tauc, R. Grigorovici, A. Vancu, Physical Status Solidi B 15 (1966) 627–637.
[50] S. Sakthivel, H. Kisch, Angewandte Chemie International Edition 42 (2003) 4908–4911.

[51] D. Sun, J. Du, Z. Liu, C. Tao, J. Zhai, Spectroscopy and Spectral Analysis 31 (2011) 525–529.
[52] B.K. Vijayan, N.M. Dimitrijevic, D. Finkelstein-Shapiro, J. Wu, K.A. Gray, ACS Catalysis 2 (2011) 223–229.
[53] Z. Li, B. Gao, G.Z. Chen, R. Mokaya, S. Sotiropoulos, G. Li Puma, Applied Catalysis B: Environmental 110 (2011) 50–57.
[54] B. Gao, G.Z. Chen, G. Li Puma, Applied Catalysis B: Environmental 89 (2009) 503–509.
[55] M. Thommes, B. Smarsly, M. Groenewolt, P.I. Ravikovitch, A.V. Neimark, Langmuir 22 (2005) 756–764.
[56] F. Kleitz, T. Czuryszkiewicz, L.A. Solovyov, M. Lindén, Chemistry of Materials 18 (2006) 5070–5079.
[57] J.C. Groen, L.A.A. Peffer, J. Pérez-Ramıírez, Microporous and Mesoporous Materials 60 (2003) 1–17.
[58] Y. Wan, X. Cui, Z. Wen, Journal of Hazardous Materials 198 (2011) 216–223.
[59] Z. Zhang, Y. Xu, X. Ma, F. Li, D. Liu, Z. Chen, F. Zhang, D.D. Dionysiou, Journal of Hazardous Materials 209–210 (2012) 271–277.
[60] Y. Li, X. Li, J. Li, J. Yin, Water Research 40 (2006) 1119–1126.